Chinese Chemical Letters 34 (2023) 108640

Contents lists available at ScienceDirect

Chinese Chemical Letters

journal homepage: www.elsevier.com/locate/cclet

Electrolyte and interphase engineering through solvation structure regulation for stable lithium metal batteries

Hai Su[a], Haikuo Zhang[b], Zifeng Chen[a], Mengjie Li[a], Jiwei Zhao[a], Haiyan Xun[a], Jie Sun[c], Yunhua Xu[a,*]

[a] School of Materials Science and Engineering, Key Laboratory of Advanced Ceramics and Machining Technology (Ministry of Education), and Tianjin Key Laboratory of Composite and Functional Materials, Tianjin University, Tianjin 300072, China
[b] State Key Laboratory of Silicon Materials, School of Materials Science and Engineering, Zhejiang University, Hangzhou 310027, China
[c] Key Laboratory for Green Chemical Technology of Ministry of Education, School of Chemical Engineering and Technology, Tianjin University, Tianjin 300072, China

ARTICLE INFO

Article history:
Received 4 May 2023
Revised 15 May 2023
Accepted 31 May 2023
Available online 4 June 2023

Keywords:
Lithium metal batteries
Lithium nitrate
Trimethyl phosphate
Solvation structures
Solid-electrolyte interphases

ABSTRACT

Lithium metal batteries (LMBs) are considered to be one of the most promising high-energy-density battery systems. However, their practical application in carbonate electrolytes is hampered by lithium dendrite growth, resulting in short cycle life. Herein, an electrolyte regulation strategy is developed to improve the cyclability of LMBs in carbonate electrolytes by introducing $LiNO_3$ using trimethyl phosphate with a slightly higher donor number compared to NO_3^- as a solubilizer. This not only allows the formaion of Li^+-coordinated NO_3^- but also achieves the regulation of electrolyte solvation structures, leading to the formation of robust and ion-conductive solid-electrolyte interphase films with inorganic-rich inner and organic-rich outer layers on the Li metal anodes. As a result, high Coulombic efficiency of 99.1% and stable plating/stripping cycling of Li metal anode in Li||Cu cells were realized. Furthermore, excellent performance was also demonstrated in Li||$LiNi_{0.83}Co_{0.11}Mn_{0.06}O_2$ (NCM83) full cells and Cu||NCM83 anode-free cells using high mass-loading cathodes. This work provides a simple interphase engineering strategy through regulating the electrolyte solvation structures for high-energy-density LMBs.

High-energy-density rechargeable batteries have attracted great attention due to the ever-increasing demand for portable electronics, electric vehicles and grid storage systems [1,2]. Unfortunately, the prevailing Li-ion batteries cannot provide satisfy energy density. One of the main limiting factors is the graphite anode that has a low theoretical specific capacity of 372 mAh/g [3]. With a high theoretical specific capacity (3860 mAh/g) and the lowest redox potential (−3.04 V *versus* standard hydrogen electrode), Li metal is regarded as the ultimate anode for the next-generation high-energy-density rechargeable batteries [4,5]. However, Li metal anode always suffers from Li dendrite growth upon cycling that causes poor electrochemical performance (including low Coulombic efficiency and rapid capacity decay) and serious safety hazards. There issues are highly related to unsuitable electrolytes, such as commercial carbonate electrolytes that contain reactive organic solvents and are electrochemically unstable at low voltages, severely hampering the practical application of LMBs [6–8].

Li metal has a higher Fermi energy level than the lowest unoccupied molecular orbital (LUMO) level of electrolytes, leading to spontaneous reactions between Li metal and electrolyte when they come into contact. The resulting products would form solid-electrolyte interphase (SEI) films on the surface of the Li metal anode. The SEI layers play a key role in preventing the electrolyte from continuously reacting, protecting the Li metal anode, and improving the electrochemical performance [9,10]. Therefore, it is critical to build high quality SEI films to realize high performance LMBs. In general, robust SEI films should contain a large amount of inorganic-rich species, uniform thickness and component distribution, and high ionic conductivity to promote even lithium plating/stripping and suppress the growth of lithium dendrites [11–14]. It was found that the solvation structures of electrolytes play a key role in forming and adjusting the physical and chemical properties of the SEI films. For example, high-concentration electrolytes (HCEs) have high salt-to-solvent mole ratios, which greatly reduce the free solvent molecules, change the solvation structure, and have anions involved in the solvation sheath. The solvated anions are involved in electrolyte reduction and SEI film formation to produce inorganic-rich interphases and improve Li plating/stripping

* Corresponding author.
E-mail address: yunhua.xu@tju.edu.cn (Y. Xu).

https://doi.org/10.1016/j.cclet.2023.108640
1001-8417/

cycling performance [15–17]. However, HCEs have high viscosities, poor wettability against electrodes and separators, and high costs, which hinder their practical application [18]. Although these issues can be mitigated by introducing non-solvating co-solvents to form localized HCEs (LHCEs), the practical application is still facing significant challenges [19–22]. Fluorinated electrolytes were also reported to be capable of forming robust LiF-rich SEI films. The high mechanical strength and high interfacial energy of LiF can induce a stable Li plating/stripping with high Coulombic efficiency [23–28].

The solvation structures and SEI films can also be regulated by adding additives to the electrolytes [29–34]. Fluoroethylene carbonate (FEC) has been demonstrated as a promising additive for constructing robust SEI films by producing LiF during the reduction process [35,36]. However, there still exists significant challenges in preventing electrolyte decomposition due to the incorporation of solvent molecules into the coordination structure. $LiNO_3$ is a widely-investigated salt additive for stabilizing Li metal anode [37–40]. NO_3^- has a high donor number (DN), getting them into solvation structure and producing nitrides/oxides-containing SEI films that are uniform and have a high ionic conductivity during electrolyte reduction [41]. However, $LiNO_3$ has a poor solubility of $\sim 10^{-5}$ g/mL in carbonate electrolytes due to the strong cation-anion interaction [42,43], making it incompatible with high-voltage oxide cathodes ($\geq$4.3 V). To improve the solubility of $LiNO_3$ in carbonate electrolytes, solubilizers such as Lewis acids [44–47] and high DN solvents [48–54] were often used,. Although the improved electrochemical performance of LMBs using high DN solvents was achieved, the inappropriate high DN solvents lead to the formation of free NO_3^- [55] and affect the oxidation stability of carbonate electrolyte [51,52]. Therefore, it is highly desirable to design new electrolytes that are compatible with both Li metal anodes and high-voltage cathodes, can form sustainable electrode-electrolyte interphases and have high ionic conductivity.

Herein, an effective strategy is developed by introducing $LiNO_3$ into the carbonate electrolyte and regulating the solvation structure by using a solubilizer of TMP. The slightly higher DN of TMP than NO_3^- allows the formation of Li^+-coordinated NO_3^-. Solvated NO_3^- in the inner shell of the solvation sheath have lower lowest unoccupied molecular orbital (LUMO) energy levels, leading to prior reduction to the solvents, and thus forming robust SEI films to protect Li metal anode. In addition, TMP has high-voltage stability, making the engineered electrolyte compatible with high voltage cathodes. As a result, high Coulombic efficiency of 99.1% and stable plating/stripping cycling of Li metal anode were realized in Li||Cu cells using the engineered carbonate electrolyte. Excellent performance was also demonstrated in Li||NCM83 full cells using high mass-loading NCM83 cathode, with a high capacity retention of 76.0% after 200 cycles. Furthermore, good cycling performance was also achieved in anode-free cells.

The DN of solvents plays an important role in determining the solubility of salts in solvents. High DN solvents have a strong ability to dissociate ion pairs due to the strong interaction with cations [48]. Ethylene carbonate (EC), ethyl methyl carbonate (EMC), and FEC solvents have DNs of 16.4, 16.6, and 9.1 kcal/mol, respectively, which are much lower than 21.1 kcal/mol of NO_3^- (Table S1 in Supporting information) [56], resulting to a poor solubility of $LiNO_3$ in these solvents. Therefore, a large amount of white precipitates was observed when a designed amount of $LiNO_3$ at a concentration of 0.2 mol/L was added to the baseline carbonate electrolyte (1 mol/L $LiPF_6$ EC-EMC (1:1, v/v), denoted as BCE) (Fig. S1a in Supporting information), demonstrating a poor solubility of $LiNO_3$ in carbonate electrolytes. To improve the solubility of $LiNO_3$ in carbonate electrolytes, TMP that has a high DN (23.0 kcal/mol) was used as a solubilizer. A high concentration of 4 mol/L can be obtained, confirming a high solubility of $LiNO_3$ in TMP (Fig. 1a). Density functional theory calculations were performed to investigate the interactions

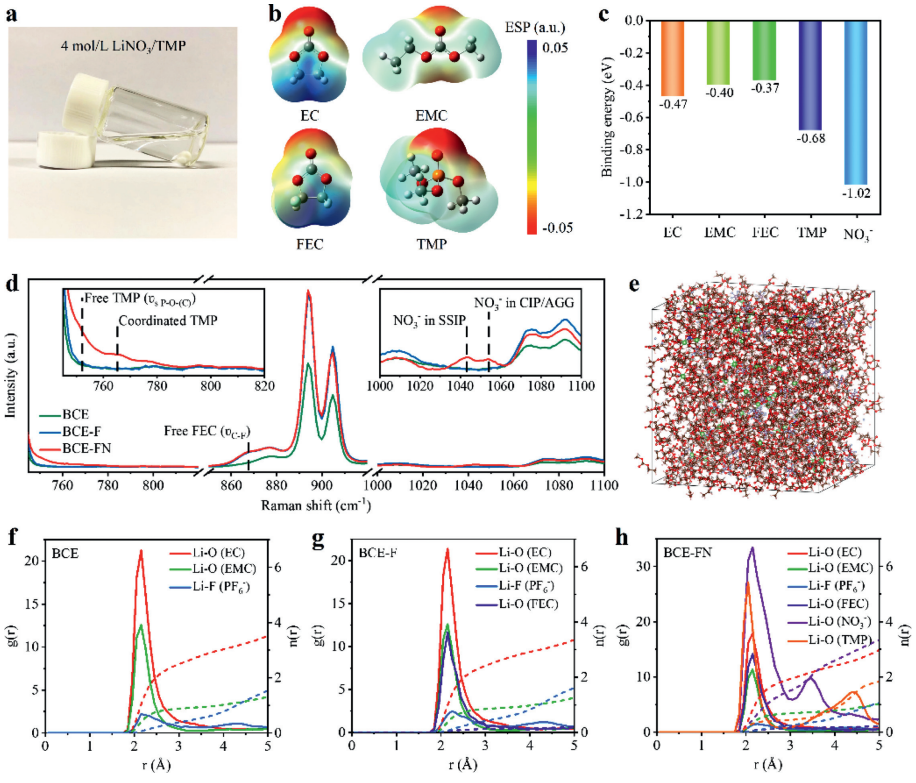

Fig. 1. Characterization of the solvation structure of different electrolytes. (a) Digital image of 4 mol/L $LiNO_3$/TMP. (b) ESP mapping of EC, EMC, FEC and TMP. (c) Binding energies of EC, EMC, FEC and TMP solvents and NO_3^- with Li^+. (d) Raman spectra of BCE, BCE-F and BCE-FN. The insets are the enlarged views of the Raman spectra at 745–820 cm^{-1} and 1000–1100 cm^{-1}. (e) Snapshots of the MD simulated box of BCE-FN. Radical distribution functions and cumulative coordination numbers in (f) BCE, (g) BCE-F and (h) BCE-FN.

between the solvent molecules and Li^+. The electrostatic potential (ESP) mapping indicates that more negative charge is concentrated on O atoms for TMP than for EC, EMC and FEC (Fig. 1b), which is conducive to the coordination of TMP with Li^+. This is confirmed by the lowest binding energy of −0.68 eV for TMP (Fig. 1c). Using TMP as a solubilizer, a $LiNO_3$-containing electrolyte was prepared by adding 5 vol% 4 mol/L $LiNO_3$/TMP solution to BCE with 5 vol% FEC, denoted as BCE-FN. For comparison, the carbonate electrolyte with 5 vol% FEC in BCE is also prepared, denoted as BCE-F. These electrolytes are both clear and transparent without precipitation, even after storage for more than one week (Fig. S1b in Supporting information), indicating highly stable interactions between Li^+, anions and solvents after the introduction of TMP.

The evolution of the solvation structures of the carbonate electrolytes upon addition of $LiNO_3$, TMP and FEC was characterized by Raman spectroscopy (Fig. 1d). For BCE-F and BCE-FN, a peak at 866 cm^{-1} is assigned to the C-F stretching vibration ($\nu_{C\text{-}F}$) of free FEC molecules [57]. When 4 mol/L $LiNO_3$/TMP is added, two additional bands arise at 752 and 765 cm^{-1}, which are identified as symmetric stretching vibration of P-O-(C) in free TMP molecule and coordinated TMP, respectively [58]. Meanwhile, two bands at 1042 and 1054 cm^{-1} were detected, which are attributed to the interaction of NO_3^- with Li^+ in the form of solvent-separated ion pair and contact ion pair/aggregate, respectively [40]. Classical molecular dynamics (MD) simulations were further performed to investigate the solvation structures of the carbonate electrolytes with and without additives. For BCE, the solvation sheath is mainly composed of EC and EMC molecules, as shown in the snapshot of the MD simulated box (Fig. S2a in Supporting information). The solvent-dominated solvation structure tends to produce organic-rich and non-uniform SEI films [59]. For BCE-F, FEC is also involved in the solvation structure (Fig. S2b in Supporting information), generating LiF and improving the quality of SEI films [60]. Impressively, it was found that NO_3^- can be involved in the solvation sheath in BCE-FN (Fig. 1e). The plots of radical distribution functions and coordination numbers (CNs) are presented in Figs. 1f-h. In BCE and BCE-F, the prominent peaks of EC and EMC at 2.15 Å show that EC and EMC molecules dominate the Li^+ solvation sheath. The CNs of EC, EMC and PF_6^- in BCE are 2.53, 0.89 and 0.40, respectively. Although FEC participates in the solvation of Li^+ in BCE-F, as revealed by the peaks at 2.15 Å, the coordination environment does not change significantly. The calculated CNs of EC, EMC, PF_6^- and FEC are 2.45, 0.86, 0.43 and 0.12, respectively. In sharp contrast, for BCE-FN, NO_3^- and TMP appear at 2.15 and 2.05 Å, respectively, implying that NO_3^- and TMP have stronger solvation ability and are incorporated into first solvation shell of Li^+. In addition, the intensities of the EC peak at 2.15 and the EMC peak at 2.15 Å are significantly reduced, implying reduced coordination interactions between Li^+ and EC/EMC. The CNs of EC, EMC, PF_6^-, FEC, NO_3^- and TMP are calculated to be 1.95, 0.69, 0.26, 0.14, 1.54 and 0.45, respectively. The representative configurations of the solvation structures of Li^+ in different electrolytes are illustrated in Fig. S3 in Supporting information. The solvated NO_3^- and FEC molecules in the inner shell of the solvation sheath have lower LUMO energy levels (Fig. S4 in Supporting information), leading to a prior reduction to EC/EMC during the discharge process. This will generates inorganic species and improves the quality of SEI films.

To evaluate the effects of additives on the electrochemical behavior of Li plating/stripping, Li||Cu and Li||Li cells were assembled and tested. With BCE-FN, the Li||Cu cells show a Li nucleation overpotential of 23.2 mV and a Li growth overpotential of 19.2 mV at the initial stage of Li deposition (Fig. 2a), much smaller than those with BCE (62.3 and 66.3 mV) and BCE-F (43.1 and 36.8 mV). This demonstrate that the introduction of FEC and $LiNO_3$ can effectively

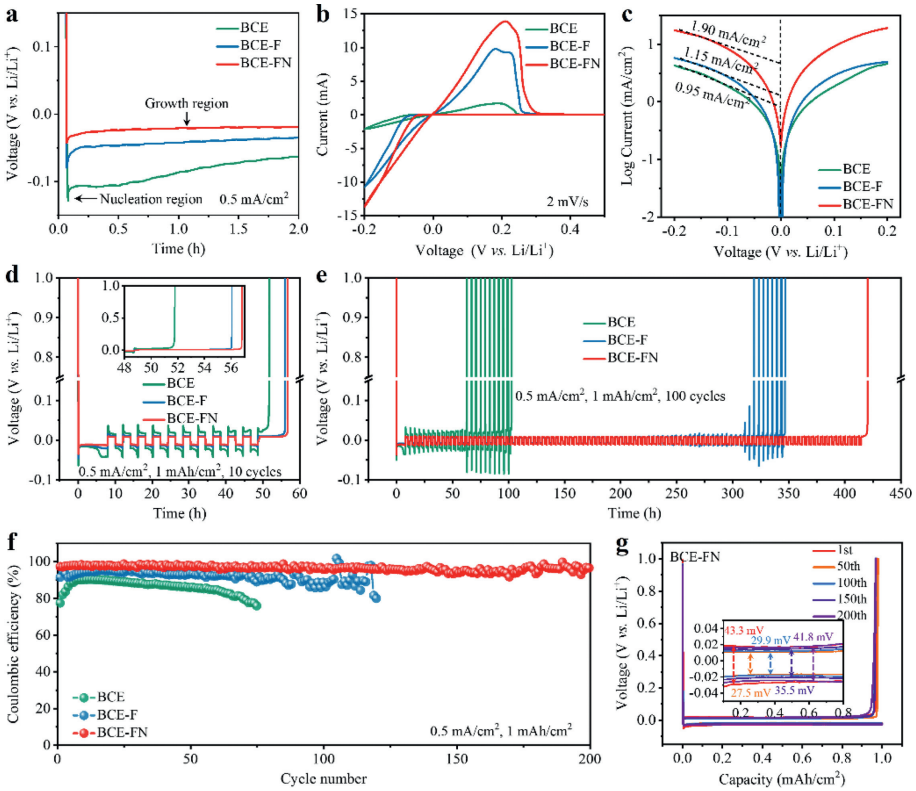

Fig. 2. Li plating/stripping behavior in different electrolytes. (a) Li nucleation and deposition overpotentials at 0.5 mA/cm^2. (b) CV curves of Li||Cu cells. (c) Tafel plots for Li plating/stripping in Li||Li cells. Li plating/stripping profiles over (d) 10 and (e) 100 cycles in Li||Cu cells at 0.5 mA/cm^2 and 1 mAh/cm^2. (f) Coulombic efficiency of Li||Cu cells at 0.5 mA/cm^2 and 1 mAh/cm^2. (g) Voltage profiles of Li||Cu cells at different cycles in BCE-FN. Inset is the magnified view of the Li plating/stripping overpotentials at different cycles.

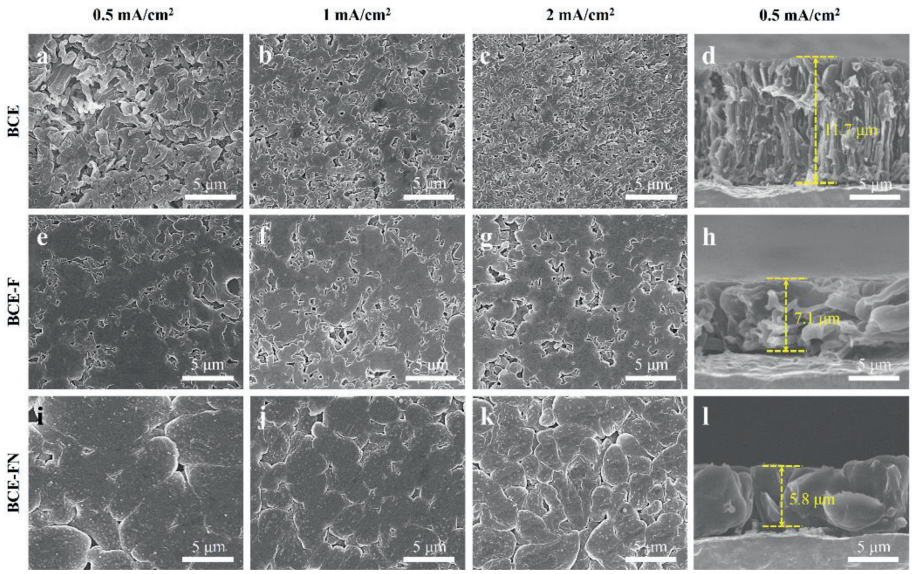

Fig. 3. Li plating morphologies on Cu substrate in different electrolytes. Top view SEM images of the plated Li at (a, e, i) 0.5 mA/cm^2, (b, f, i) 1 mA/cm^2 and (c, g, k) 2 mA/cm^2 in (a-c) BCE, (e-g) BCE-F and (i-k) BCE-FN with a constant Li capacity of 1 mAh/cm^2. The corresponding cross-sectional SEM images of the plated Li at 0.5 mA/cm^2 in (d) BCE, (h) BCE-F and (l) BCE-FN.

regulate the Li deposition behavior with a smaller barrier. The difference between the electrolytes was also indicated by the cyclic voltammetry (CV) curves of Li||Cu cells at a scan rate of 2 mV/s (Fig. 2b and Fig. S5 in Supporting information). BCE-FN shows a much larger Li plating/stripping current than BCE and BCE-F, suggesting a faster kinetics in BCE-FN. Furthermore, the Tafel plots of Li||Li cells at 1 mV/s show that BCE-FN has a high exchange current density of 1.90 mA/cm^2, much higher than BCE (0.95 mA/cm^2) and BCE-F (1.15 mA/cm^2) (Fig. 2c), respectively, indicating an enhanced Li^+ transfer capability at the electrode/electrolyte interface for BCE-FN.

Furthermore, Li plating/stripping cycling performance was examined in Li||Cu cells at 0.5 mA/cm^2 and 1 mAh/cm^2. A low average Coulombic efficiency of 82.3% over 10 cycles was displayed for BCE. While it is dramatically improved for BCE-F (97.6%) and BCE-FN (99.1%) (Fig. 2d), implying that the side reactions are significantly suppressed by BCE-F and BCE-FN. Similarly, a higher stability of the plating/stripping cycling was obtained over 100 cycles with a high average Coulombic efficiency of 98.9% for BCE-FN (Fig. 2e). In contrast, the cells with BCE failed to work after 13 cycles. Coulombic efficiency was further tested in a long-term cycling at 0.5 mA/cm^2 and 1 mAh/cm^2. As shown in Fig. 2f, BCE suffered a quick drop to less than 75.8% after 75 cycles. For BCE-F, a higher Coulombic efficiency of 94.5% is displayed, but the cells delivered an undesirable cycling stability. For BCE-FN, a much higher Coulombic efficiency of 98.3% was obtained over 200 cycles, highlighting the effective suppression of Li dendrite growth and side reactions of the electrolyte. The enhancement in Li plating/stripping performance is further revealed by the voltage curves and the corresponding overpotentials at different cycles (Fig. 2g and Fig. S6 in Supporting information).

The morphologies of the deposited Li on Cu substrates at different current densities with a capacity of 1 mAh/cm^2 in different electrolytes were characterized using scanning electron microscope (SEM). At a current density of 0.5 mA/cm^2, a dendritic Li morphology was displayed in BCE (Fig. 3a). Such structure exposes a large surface area to electrolytes, causing aggravated side reactions, and would lead to significant safety hazard. At higher current densities of 1 and 2 mA/cm^2, poorer performance was observed with a more severe porous structure (Figs. 3b and c). The cross-sectional SEM image of the cycled Li metal anodes clearly shows a highly loose whisker-like internal structure (Fig. 3d). The thickness reaches 11.7 μm, two times thicker than the theoretical value of 4.9 μm. In BCE-F, although the improved morphology was obtained with increased Li dendrite sizes and reduced porosity (Figs. 3e-g), there is still exists obvious porous microstructure with a thickness of 7.1 μm (Fig. 3h). In sharp contrast, a compact, large granules and dendrite-free morphology was achieved in BCE-FN (Figs. 3i-k). Even at a high current density of 2 mA/cm^2, a dense structure of Li was displayed. The thickness of the deposited Li is 5.8 μm, which is close to the theoretical value (Fig. 3l). These results show that the engineered carbonate electrolyte can effectively suppress the dendrite growth of Li metal anode. Furthermore, the morphology evolution with Li plating/stripping on the Cu substrates at 0.5 mA/cm^2 was also investigated in different electrolytes (Fig. S7 in Supporting information). When the Li deposition capacity was increased from 1 mAh/cm^2 to 4 mAh/cm^2, no obvious morphology change occurred except for the increase in Li dendrite size for BCE and BCE-F. The Li became more porous after Li stripping of 2 mAh/cm^2, and the porous structure remained after Li stripping to 1 V, implying a large amount of SEI films and "dead Li" were formed. In contrast, for BCE-FN, there is no Li dendrites were formed even at 4 mAh/cm^2 Li plating, and a dense morphology was well maintained after complete Li stripping to 1 V.

The Li plating/stripping reversibility in BCE and BCE-FN was further examined using Li||Li cells by an *in situ* visual experiment using an optical microscope. In BCE, a mossy morphology appeared and grew quickly with Li plating (Fig. 4a). After Li stripping, the mossy Li turned black due to the generation of "dead Li". In contrast, no obvious morphology change was observed in BCE-FN. A neat surface and shining color were observed during both the plating and stripping processes, demonstrating the effective protection of Li metal anode in BCE-FN. The long-term Li plating/stripping stability in different electrolytes was investigated. In BCE, the cells suffered from short circuit with a rapid increase of overpotential after 620 h of cycling at 1 mA/cm^2 and 1 mAh/cm^2, indicating severe dendrite growth and formation of SEI films. In contrast, excellent cycling stability with a small overpotential of 31.2 mV was achieved over 800 h cycling in BCE-FN (Fig. 4b). When

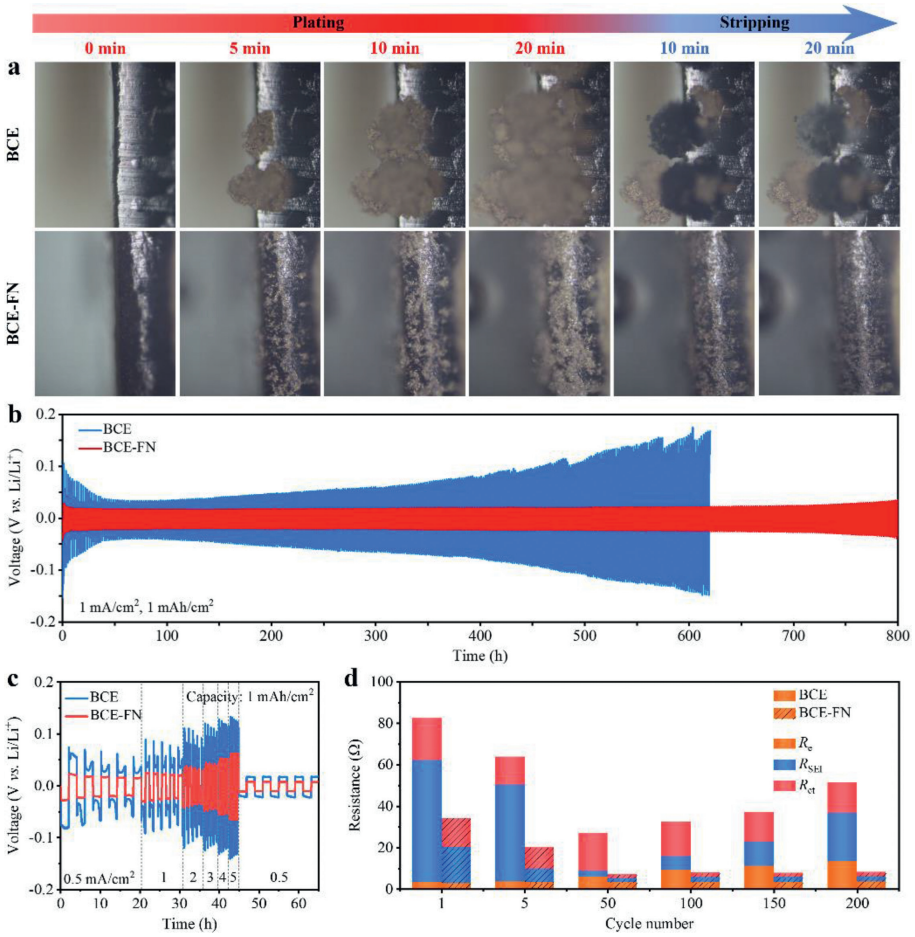

Fig. 4. Li plating/stripping performance in Li||Li symmetric cells with different electrolytes. (a) *In situ* optical microscope images with different plating and stripping time. (b) Cycling stability at 1 mA/cm^2 and 1 mAh/cm^2. (c) Rate performance at various current densities with a constant capacity of 1 mAh/cm^2. (d) Comparison of the R_e, R_{SEI}, and R_{ct} for the Li||Li cells at different cycles at 1 mA/cm^2 and 1 mAh/cm^2 in different electrolytes.

the capacity was increased to 2 and 4 mAh/cm^2, stable and long cycling was still obtained (Fig. S8 in Supporting information). More importantly, BCE-FN also enables enhanced rate capability with much smaller overpotentials as the current density ranged from 0.5 mA/cm^2 to 5 mA/cm^2 (Fig. 4c). No apparent voltage increase occurred over 300 h cycling even at a high current density of 2 mA/cm^2 (Fig. S9 in Supporting information).

The Li plating/stripping behavior in different electrolytes was further investigated by electrochemical impedance spectroscopy (EIS). All EIS curves show a semicircle in the high-frequency region (Figs. S10a and b in Supporting information), which is related to the resistance of the Li^+ diffusion through SEI films (R_{SEI}) [61]. In BCE, a large initial R_{SEI} of 117.2 Ω was measured with a continuous increase to 210.4 Ω during 18 h aging. In contrast, a significantly reduced and stable R_{SEI} was obtained in BCE-FN. It increased slightly from 39.8 Ω to 47.8 Ω in the initial 3 h aging, and remained stable thereafter (Fig. S10c in Supporting information). These results further demonstrate that the engineered electrolyte is capable of constructing a highly stable and Li^+ conductive SEI film on the Li metal anode. The improved stability was also revealed by the impedance evolution during Li plating/stripping cycle at 1 mA/cm^2 and 1 mAh/cm^2. Although an impedance decrease was observed in the initial 50 cycles in both electrolytes, BCE-FN showed smaller impedance than BCE (Fig. 4d and Fig. S11 in Supporting information). With cycling, the impedance gradually increased in BCE, indicating a growing SEI film caused by the continuous side reactions of electrolyte on the surface of Li metal anode. In contrast, stable impedance was displayed for BCE-FN, infesting a stable SEI film. Therefore, BCE-FN can protect the Li metal anode from Li dendrite growth by forming a stable and Li^+ conductive SEI film, thus promising a stable Li plating/stripping cycling performance.

The compositions of the SEI films formed on the Li metal electrodes in different electrolytes were investigated using in-depth X-ray photoelectron spectroscopy (XPS). The Li metal electrodes were retrieved from Li||Li cells after 10 plating/stripping cycles at 1 mA/cm^2 and 1 mAh/cm^2 and etched by argon ions for different time. Both of them show pronounced C 1s signals that are derived from the decomposition of solvents (Figs. S12a and c in Supporting information). But it is much stronger for BCE than BCE-FN, even after etching, suggesting more organic species were produced in the former. After 10 min etching, a weak C-Li peak was detected for the electrode in BCE, while a much stronger peak was measured in BCE-FN after 2 min etching, demonstrating a thicker SEI film formed in BCE. LiF was also detected for both electrolytes as shown by the F 1s spectra (Figs. 5a and e). In BCE, it was derived from the decomposition of $LiPF_6$. This is further indicated by the production of Li_xPF_y and $Li_xPO_yF_z$ in the P 2p spectra (Fig. S12b in Supporting information). No significant change in intensity of the F 1s peaks was measured after etching, indicating continuous decomposition of $LiPF_6$. While in BCE-FN, LiF was produced by the decomposition of FEC. The peaks of LiF became stronger with etching, revealing a gradient component distribution from the outer to the inner layer of the SEI films. No P-containing species were de-

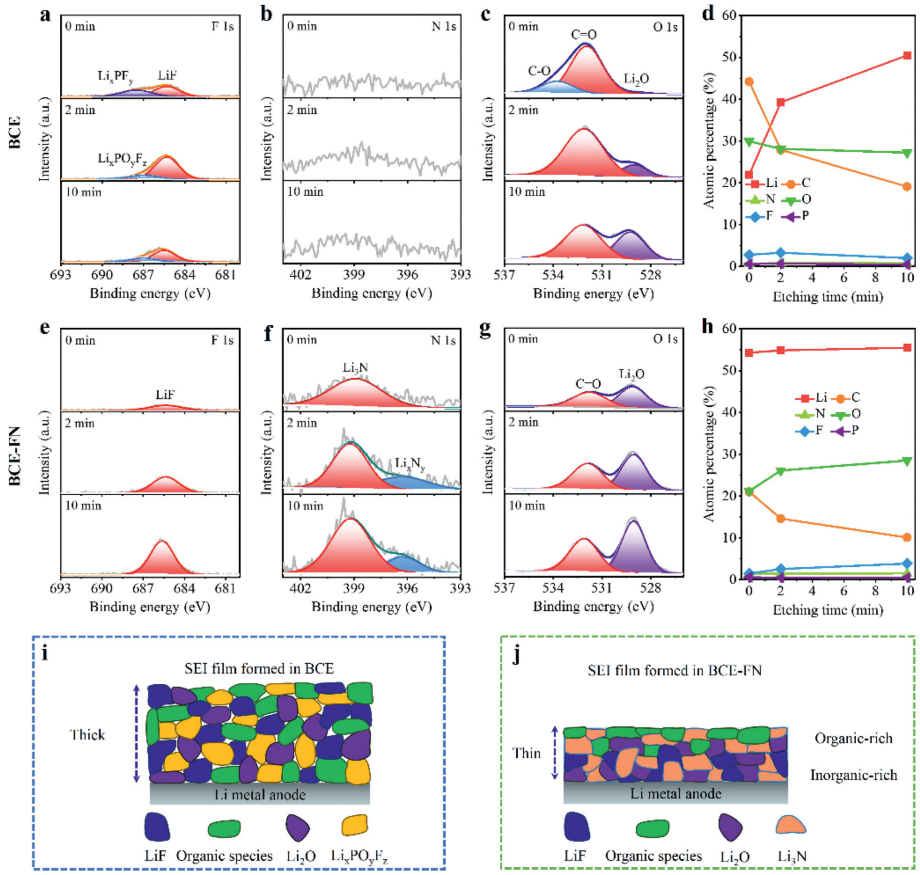

Fig. 5. Component analysis of the SEI films formed in BCE and BCE-FN. (a, e) F 1s, (b, f) N 1s and (c, g) O 1s XPS spectra with different etching time. Atomic percentages of different elements at different etching time in (d) BCE and (h) BCE-FN. Schematic illustration of the SEI films formed in (i) BCE and (j) BCE-FN.

tected (Fig. S12d in Supporting information), showing that the reduction of $LiPF_6$ in BCE-FN was effectively suppressed. In addition, for the N 1s spectra (Figs. 5b and f) and O 1s spectra (Figs. 5c and g), the SEI film in BCE-FN shows conspicuous Li_xN_y and Li_3N peaks at 396.3 and 399.2 eV and stronger Li_2O peaks at 531.8 eV with gradient distributions compared to BCE. These species in BCE-FN are mainly derived from the reduction of $LiNO_3$ because NO_3^- has a strong coordination effect with Li^+ and tends to be reduced during the discharge process [62,63].

The gradient component distributions of the SEI films in BCE and BCE-FN were analyzed. In BCE, a high carbon content of 44.2 at% was measured on the pristine SEI films (Fig. 5d), indicating that a large amount of organic components were produced. Even after 10 min etching, it is still up to 19.1 at%, revealing that the thick SEI films are composed of a high proportion of organic species throughout the whole layer. Therefore, BCE underwent severe and continuous side reactions. In contrast, a much lower content of C content (21.0 at%) was measured for the pristine SEI film in BCE-FN (Fig. 5h), indicating a lower fraction of organic components in the outer layer of SEI. After 10 min etching, it declined to only 10.1 at%, suggesting less organic species in the inner layer. Besides, high contents of F and O were measured for the pristine samples in BCE-FN, ascribes to high ratios of inorganic species in the outer layer of SEI films. Meanwhile, they became more abundant in the inner layer, testifying a gradient distribution. The inorganic-rich inner layer provides a high ionic conductivity, high interfacial energy and high mechanical strength, which effectively regulates Li plating [64]. While the organic-rich outer layer has good flexibility, providing a high tolerance to structural deformation [65]. Therefore, the sustainable SEI films promise an effective protection for the Li metal anode and ensure high performance of LMBs. The different SEI structures in BCE and BCE-FN are also schematically illustrated in Figs. 5i and j.

The engineered electrolyte of BCE-FN also shows a good stability at high voltage. The electrochemical window of the engineered electrolyte was examined by linear sweep voltammetry measurement in a cell using carbon (Super P) electrodes. The BCE was also tested as a control. Excellent oxidation stability above 4.5 V was obtained (Fig. S13 in Supporting information), promising good electrochemical performance for high voltage cathodes. This was investigated in coin-type cells using 50 μm Li metal anodes and NCM83 cathodes with areal capacities of 1.8 and 4.3 mAh/cm^2. CV curves were collected at a scan rate of 0.1 mV/s between 2.7 V and 4.3 V for the 1.8 mAh/cm^2 cathode. No severe oxidation peak was observed except for the three pairs of phase transition peaks for the NCM83 cathode (Fig. S14 in Supporting information), verifying the good compatibility of BCE-FN with the NCM83 cathode. The cycling performance was tested at a charge/discharge rate of 0.5 C (1 C = 200 mA/g) between 2.7 V and 4.3 V (Fig. 6a). BCE suffered a rapid capacity and Coulombic efficiency degradation after 50 cycles. In sharp contrast, BCE-FN delivered significantly enhanced performance with a high Coulombic efficiency of 99.7% and 76.0% capacity retention after 200 cycles, demonstrating the superiority of the engineered electrolyte. Furthermore, BCE-FN shows smaller and stable voltage polarization (Figs. 6b and c) as well as better rate capability (Fig. 6d and Fig. S15 in Supporting information) than BCE, verifying thin and stable SEI films with higher ionic conductivity were formed in BCE-FN. At a high cur-

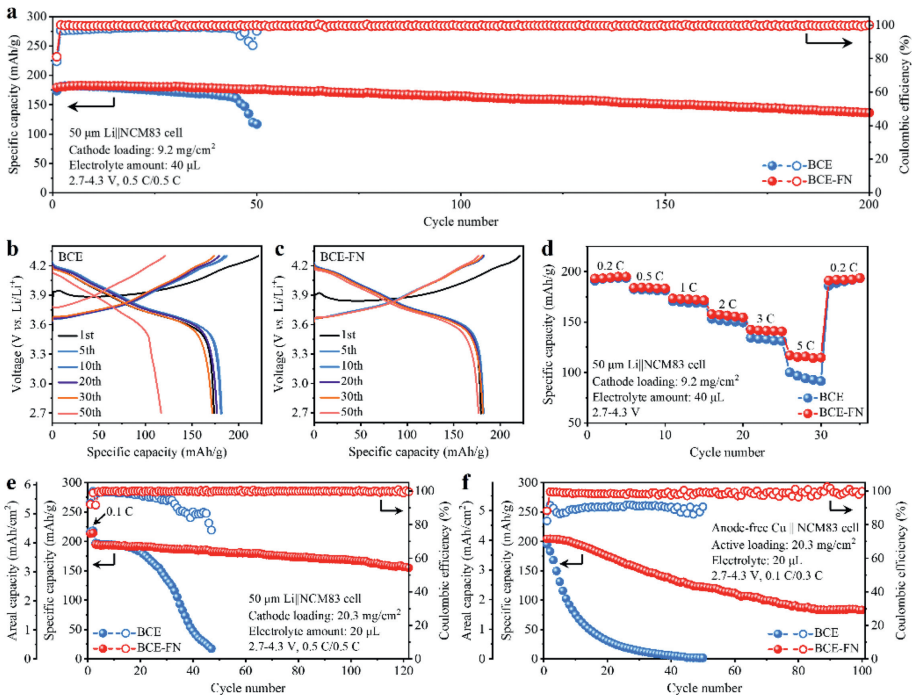

Fig. 6. Electrochemical performance of Li||NCM83 cells in different electrolytes between 2.7 V and 4.3 V. (a) Cycling stability, the voltage profiles during 50 cycles in (b) BCE and (c) BCE-FN at 0.5 C, and (d) rate capability using 50 μm Li metal anodes, NCM83 cathodes with a mass loading of 9.2 mg/cm^2 and an electrolyte amount of 40 μL. (e) Cycling stability of Li||NCM83 cells at 0.5 C using 50 μm Li metal anodes, NCM83 cathodes with a mass loading of 20.3 mg/cm^2 and an electrolyte amount of 20 μL. (f) Cycling stability of anode-free Cu||NCM83 cells at the charge/discharge rates of 0.1 C/0.3 C using NCM83 cathodes with a mass loading of 20.3 mg/cm^2 and an electrolyte amount of 20 μL.

rent rate of 5 C, a high discharge capacity of 115.8 mAh/g was retained.

The superiority of the engineered electrolyte was further manifested by the good performance of the NCM83 cathode with a high areal capacity of 4.3 mAh/cm^2 and limited electrolyte amount of 20 μL. With BCE-FN, the Li||NCM83 full cells can be cycled 120 times with a capacity retention of 80.2% even at a high charge/discharge rate of 0.5 C (*i.e.*, 2.0 mA/cm^2) (Fig. 6e and Fig. S16 in Supporting information). While in BCE, after 18 cycles, a rapid performance degradation occurred, indicating a fast depletion of active Li metal and electrolyte due to the severe side reactions. Furthermore, BCE-FN can sustain a high voltage. At a high cut-off voltage of 4.4 V, the Li||NCM83 full cells can still survive 110 cycles with a capacity retention of 75.8% (Fig. S17 in Supporting information). This is much higher than 3.6% capacity retention after 40 cycles for BCE. In light of the excellent stability of BCE-FN at both Li metal anode and NCM83 cathode, anode-free Cu||NCM83 cells were fabricated and tested. A high average Coulombic efficiency of 98.8% over 100 cycles was delivered, contrasting with 90.2% over 40 cycles for BCE (Fig. 6f and Fig. S18 in Supporting information). This is comparable with fluorinated electrolytes and LHCEs in anode-free cells (Table S2 in Supporting information).

In summary, an electrolyte and interphase engineering strategy is reported by introducing $LiNO_3$ into carbonate electrolytes using TMP as a solubilizer. This can form Li^+-coordinated NO_3^- and effectively regulate the electrolyte solvation structure due to the sightly higher DN of TMP than NO_3^-, and form gradient and ion-conductive SEI films with inorganic-rich inner and organic-rich outer layers to protect Li metal anodes. The engineered electrolyte shows high compatibility with Li metal anodes and high voltage cathodes. Exceptional electrochemical performance was demonstrated on Li metal anodes, NMC83 cathodes, and full LMBs. This work provides a facile interphase engineering strategy by regulating electrolyte solvation structures for high-energy-density LMBs.

Acknowledgments

This work was supported by the National Key Research and Development Program of China (No. 2019YFE0118800).

Supplementary materials

Supplementary material associated with this article can be found, in the online version, at doi:10.1016/j.cclet.2023.108640.

References

[1] M. Armand, J.M. Tarascon, Nature 451 (2008) 652–657.
[2] J.W. Choi, D. Aurbach, Nat. Rev. Mater. 1 (2016) 16013.
[3] J. Janek, W.G. Zeier, Nat. Energy 1 (2016) 16141.
[4] D. Lin, Y. Liu, Y. Cui, Nat. Nanotech. 12 (2017) 194–206.
[5] X.B. Cheng, R. Zhang, C.Z. Zhao, et al., Chem. Rev. 117 (2017) 10403–10473.
[6] X. Gao, Y.N. Zhou, D. Han, et al., Joule 4 (2020) 1864–1879.
[7] Y. Zhang, T.T. Zuo, J. Popovic, et al., Mater. Today 33 (2020) 56–74.
[8] Q. Zhao, S. Stalin, L.A. Archer, Joule 5 (2021) 1119–1142.
[9] G.M. Hobold, J. Lopez, R. Guo, et al., Nat. Energy 6 (2021) 951–960.
[10] Z. Wang, Z. Sun, J. Li, et al., Chem. Soc. Rev. 50 (2021) 3178–3210.
[11] X. Fan, L. Chen, X. Ji, et al., Chem 4 (2018) 174–185.
[12] W. Xue, Z. Shi, M. Huang, et al., Energy Environ. Sci. 13 (2020) 212–220.
[13] Q. Wang, Z. Yao, C. Zhao, et al., Nat. Commun. 11 (2020) 4188.
[14] Y. Chen, Z. Yu, P. Rudnicki, et al., J. Am. Chem. Soc. 143 (2021) 18703–18713.
[15] L. Suo, Y.S. Hu, H. Li, et al., Nat. Commun. 4 (2013) 1481.
[16] J. Qian, W.A. Henderson, W. Xu, et al., Nat. Commun. 6 (2015) 6362.
[17] L. Suo, W. Xue, M. Gobet, et al., Proc. Natl. Acad. Sci. U. S. A. 115 (2018) 1156–1161.
[18] Y. Yamada, J. Wang, S. Ko, et al., Nat. Energy 4 (2019) 269–280.
[19] S. Chen, J. Zheng, D. Mei, et al., Adv. Mater. 30 (2018) 1706102.
[20] X. Cao, X. Ren, L. Zou, et al., Nat. Energy 4 (2019) 796–805.
[21] S. Zhang, R. Li, N. Hu, et al., Nat. Commun. 13 (2022) 5431.
[22] Z. Jiang, Z. Zeng, X. Liang, et al., Adv. Funct. Mater. 31 (2020) 2005991.
[23] X. Fan, L. Chen, O. Borodin, et al., Nat. Nanotech. 13 (2018) 715–722.
[24] Z. Yu, P.E. Rudnicki, Z. Zhang, et al., Nat. Energy 7 (2022) 94–106.
[25] P. Xiao, Y. Zhao, Z. Piao, et al., Energy Environ. Sci. 15 (2022) 2435–2444.
[26] W. Zhang, Y. Guo, T. Yang, et al., Energy Storage Mater. 51 (2022) 317–326.
[27] C.C. Su, M. He, M. Cai, et al., Nano Energy 92 (2022) 106720.
[28] Y. Zhao, T. Zhou, T. Ashirov, et al., Nat. Commun. 13 (2022) 2575.

[29] X.Q. Zhang, X. Chen, L.P. Hou, et al., ACS Energy Lett. 4 (2019) 411–416.
[30] S. Kim, T.K. Lee, S.K. Kwak, et al., ACS Energy Lett. 7 (2022) 67–69.
[31] Y. Zhang, Y. Wu, H. Li, et al., Nat. Commun. 13 (2022) 1297.
[32] F. Li, J. He, J. Liu, et al., Angew. Chem. Int. Ed. 60 (2021) 6600.
[33] Z. Lu, Y. Guo, S. Zhang, et al., Adv. Mater. 33 (2021) 2101745.
[34] Q. Ma, X. Zhang, A. Wang, et al., Adv. Funct. Mater. 30 (2020) 2002824.
[35] X.Q. Zhang, X.B. Cheng, X. Chen, et al., Adv. Funct. Mater. 27 (2017) 1605989.
[36] G.X. Li, H. Jiang, R. Kou, et al., ACS Energy Lett. 7 (2022) 2282–2288.
[37] X.Q. Zhang, X. Chen, X.B. Cheng, et al., Angew. Chem. Int. Ed. 57 (2018) 5301–5305.
[38] S.J. Zhang, Z.W. Yin, Z.Y. Wu, et al., Energy Storage Mater. 40 (2021) 337–346.
[39] H. Yang, X. Chen, N. Yao, et al., ACS Energy Lett. 6 (2021) 1413–1421.
[40] X. Wang, S. Wang, H. Wang, et al., Adv. Mater. 33 (2021) 2007945.
[41] W. Zhang, Y. Lu, L. Wan, et al., Nat. Commun. 13 (2022) 2029.
[42] Y. Liu, D. Lin, Y. Li, et al., Nat. Commun. 9 (2018) 3656.
[43] Q. Shi, Y. Zhong, M. Wu, et al., Proc. Natl. Acad. Sci. U. S. A. 115 (2018) 5676–5680.
[44] C. Yan, Y.-X. Yao, X. Chen, et al., Angew. Chem. Int. Ed. 57 (2018) 14055–14059.
[45] W. Zhang, Q. Wu, J. Huang, et al., Adv. Mater. 32 (2020) 2001740.
[46] S. Liu, J. Xia, W. Zhang, et al., Angew. Chem. Int. Ed. 61 (2022) e202210522.
[47] D. Lee, S. Sun, C. Kim, et al., Appl. Surf. Sci. 572 (2022) 151439.
[48] Y. Jie, X. Liu, Z. Lei, et al., Angew. Chem. Int. Ed. 59 (2020) 3505–3510.
[49] S. Liu, X. Ji, N. Piao, et al., Angew. Chem. Int. Ed. 60 (2021) 3661–3671.
[50] N. Piao, S. Liu, B. Zhang, et al., ACS Energy Lett. 6 (2021) 1839–1848.
[51] P. Xiao, R. Luo, Z. Piao, et al., ACS Energy Lett. 6 (2021) 3170–3179.
[52] Z. Piao, P. Xiao, R. Luo, et al., Adv. Mater. 34 (2022) 2108400.
[53] Z. Zhu, Z. Liu, R. Zhao, et al., Adv. Funct. Mater. 32 (2022) 2209384.
[54] Z. Wang, Y. Wang, B. Li, et al., Angew. Chem. Int. Ed. 61 (2022) e202206682.
[55] R. Xu, X. Shen, X.X. Ma, et al., Angew. Chem. Int. Ed. 60 (2021) 4215–4220.
[56] G. Zhou, J. Yu, J. Liu, et al., Cell Rep. Phys. Sci. 3 (2022) 100722.
[57] G. Yang, I.N. Ivanov, R.E. Ruther, et al., ACS Nano 12 (2018) 10159–10170.
[58] H. Nakagawa, M. Ochida, Y. Domi, et al., J. Power Sources 212 (2012) 148–153.
[59] W. Fang, Z. Wen, L. Chen, et al., Nano Energy 104 (2022) 107881.
[60] C.C. Su, M. He, J. Shi, et al., Angew. Chem. Int. Ed. 59 (2020) 18229–18233.
[61] L.P. Hou, X.Q. Zhang, B.Q. Li, et al., Angew. Chem. Int. Ed. 59 (2020) 15109–15113.
[62] Z. Guo, X. Song, Q. Zhang, et al., ACS Energy Lett. 7 (2022) 569–576.
[63] S. Zhang, G. Yang, Z. Liu, et al., Nano Lett. 21 (2021) 3310–3317.
[64] J. Zhang, H. Zhang, L. Deng, et al., Energy Storage Mater. 54 (2023) 450–460.
[65] A.L. Michan, B.S. Parimalam, M. Leskes, et al., Chem. Mater. 28 (2016) 8149–8159.